

Phonon dephasing times determined with time-delayed, broadband CARS

F. Hempel,¹ M. Rüsing,^{2,3} F. Vernuccio,⁴ K. J. Spychala,² R. Buschbeck,¹ G. Cerullo,⁴ D. Polli,^{4,5} and L. M. Eng^{1,6}

¹*TU Dresden, Institute of Applied Physics, Nöthnitzer Strasse 61, 01187 Dresden, Germany*

²*Department of Physics, Paderborn University, Warburger Str. 100, 33098 Paderborn, Germany*

³*Institute for Photonic Quantum Systems (PhoQS), Paderborn University, Warburger Str. 100, 33098 Paderborn, Germany*

⁴*Physics Department, Politecnico di Milano, 20133 Milano, Italy*

⁵*CNR Institute for Photonics and Nanotechnology (CNR-IFN), Milan, Italy*

⁶*ct.qmat: Dresden-Würzburg Cluster of Excellence—EXC 2147, TU Dresden, 01062 Dresden, Germany*

(*Electronic mail: dario.polli@polimi.it)

(*Electronic mail: lukas.eng@tu-dresden.de)

(Dated: 13 June 2025)

Coherent Raman scattering techniques as coherent anti-Stokes Raman scattering (CARS), offer significant advantages in terms of pixel dwell times and speed as compared to spontaneous Raman scattering for investigations of crystalline materials. However, the spectral information in CARS is often hampered by the presence of a non-resonant contribution to the scattering process that shifts and distorts the Raman peaks. In this work, we apply a method to obtain non-resonant background-free spectra based on time-delayed, broadband CARS (TD-BCARS) using an intra-pulse excitation scheme. In particular, this method can measure the phononic dephasing times across the full phonon spectrum at once. We test the methodology on amorphous SiO₂ (glass), which is used to characterize the setup-specific and material-independent response times, and then apply TD-BCARS to the analysis of single crystals of diamond and ferroelectrics of potassium titanyl phosphate (KTP) and potassium titanyl arsenate (KTA). For diamond, we determine a dephasing time of $\tau = 7.81$ ps for the single sp³ peak.

I. INTRODUCTION

Spontaneous Raman (SR) micro-spectroscopy is extensively utilized in solid-state physics because the vibrational spectrum provides valuable information about numerous properties, such as crystal structure and its symmetry, the stoichiometric composition, presence of defects and dopants, ferroelectric and magnetic properties, local strain, or insights about nanoscale confinement, e.g. in nanoparticles or 2D materials^{1–11}. SR micro-spectroscopy requires little sample preparation and can be employed for 2D and even 3D mapping, when used in a confocal setup. However, a key challenge of SR is its weak scattering cross-section, which often results in long integration times of several seconds or more per spectrum, severely limiting acquisition speed and, in turn, the field of view in image applications^{12–14}. In this regard, coherent anti-Stokes Raman scattering (CARS) offers a viable alternative^{12–15}. CARS sees widespread use in microbiology for chemically-sensitive detection and imaging and has recently also been applied to solid-state crystal systems. CARS is based on a nonlinear optical scattering process, which enables integration times per spectrum in the μ s regime and below, which enables high-speed single-frequency vibrational imaging over large fields of view. This is particularly true for broadband CARS (BCARS) methods^{16–21}, which probe a full spectrum at once without the need for lengthy tuning of one or more of the involved lasers. In principle, CARS offers comparable information to SR spectroscopy, because it also provides spectral information about the phonons of a material, their frequencies and scattering efficiency, but with much

shorter integration times.

Nonetheless, CARS comes with challenges, such as the presence of a non-resonant background (NRB), which leads to distortion of the spectral information, e.g. a spectral shift, as well as asymmetric broadening of peaks^{16,17,19,22–24}. The NRB, which arises from the (broadband) electronic contribution to the nonlinear susceptibility, interferes with the resonant vibrational response and distorts the CARS spectra. This is a particular challenge for spectroscopic investigations, such as in the context of crystalline materials. Here, the information, e.g., about strain, defects, etc., is often encoded in subtle spectral changes, such as small (< 1 cm^{−1}) shifts or the (asymmetric) broadening of peaks. Therefore, to accurately extract spectral information and achieve comparability to established SR or infrared (IR) spectroscopy measurements, it is mandatory to remove the NRB and extract the pure resonant response from the CARS spectra.

Consequently, various methods have been developed to retrieve NRB-free CARS spectra. Traditionally, the recorded raw-data spectra are corrected post-measurement by using numerical phase-retrieval algorithms based on either the time-domain Kramers-Kronig²² or the maximum entropy methods²⁵, which require a measurement on non-resonant samples (e.g., glass coverslip or water) to estimate the actual NRB of the material, as well as the setup-specific transfer function. However, since the pure non-resonant CARS response of the sample cannot be measured independently, the algorithms have to account for amplitude and phase differences that need to be corrected for prior to deriving the pure resonant response. Recently, the NRB removal prob-

lem has been treated as a supervised learning problem by using deep neural networks, which provides another valuable alternative^{19,23,24} for NRB removal. These methods do not need any additional measurements on reference samples; moreover, they provide the pure vibrational spectrum in a much shorter time than the one required by NRB removal algorithms, being beneficial for CARS imaging applications.

In this work, we present an experimental implementation based on time-delayed CARS (TD-CARS) to remove the NRB in the CARS spectra without the need of any post-processing algorithm. TD-CARS^{26,27} is based on the fact that the non-resonant and resonant contributions in the CARS four-wave mixing process decay with substantially different time constants. Here, the non-resonant contribution is a response of the electronic system of a material, which dephasing is instantaneous for all intents and purposes²⁸. In contrast, the resonant contribution in CARS is a response of the much slower moving atomic contributions (phonons) to the nonlinear susceptibility, which has dephasing times in the order of ps or longer, which is inversely proportional to the linewidth. Therefore, if a sufficient time-delay is introduced between the pump and probe pulses in the CARS process, a true NRB-free CARS spectrum is obtained.

Our experimental implementation combines broadband CARS and time-delayed CARS (TD-BCARS) to measure NRB-free spectra across a broad Raman range up to approximately 1300 cm^{-1} , which is sufficient for most crystalline materials, which rarely have phonon frequencies higher than 1000 cm^{-1} . We first characterize the NRB-dephasing times and their relation to the pump and probe pulses, before demonstrating NRB-free CARS spectra. Furthermore, we use a controlled time-delay to determine phonon dephasing times, i.e. the lifetimes of the coherently excited vibrational modes, of crystalline materials across the full spectrum up to approximately 1300 cm^{-1} at once. This latter information might be particularly interesting for research on solid-state materials, because the lifetimes of the coherently excited vibrations can be expected to be correlated, for example, with crystal quality or local material changes, e.g. by doping, etching, or other processes.

II. THE PRINCIPLES OF TIME-DELAYED CARS

CARS is a third-order nonlinear ($\chi^{(3)}$) four-wave mixing process involving three interactions with fields at the pump frequency ω_{pu} , the Stokes frequency ω_s , and the probe frequency ω_{pr} , resulting in the emission of a signal at the anti-Stokes frequency $\omega_{as} = \omega_{pu} - \omega_s + \omega_{pr}$. In principle, CARS can use three distinct laser wavelengths for excitation. The intensity of the emitted anti-Stokes frequency light ω_{as} is drastically enhanced compared to non-resonant frequency combinations, whenever the difference between pump and Stokes frequency $\omega_{pu} - \omega_s = \Omega$ matches a vibrational frequency of a phonon mode Ω , due to resonances in the frequency-dependent third-order nonlinear susceptibility $\chi^{(3)}$. Often, the pump and probe frequencies are chosen to be provided by the same laser, i.e. $\omega_{pr} = \omega_{pu}$, which also ensures tem-

poral overlap between these beams. As only one separate Stokes frequency ω_s is required, this process is referred to as two-color CARS (2C-CARS) spectroscopy and is schematically shown in Fig. 1a). For that case the pump laser usually features a comparatively narrowband (NB-pump) spectrum. This is the most common procedure to excite and probe the vibrational modes in CARS implementations. In the case of BCARS, a broadband Stokes spectrum is used to generate broadband anti-Stokes components that contain the information from many vibrational modes at once²⁹. However, in these implementations, as pump and probe frequencies are provided by the same laser, the excitation and probing occurs instantaneously and cannot be temporally separated. Therefore, TD-CARS is not possible with a 2C-(B)CARS setup.

To allow for time-delayed CARS in broadband implementations, a three-color CARS (3C-CARS) excitation scheme is necessary as shown in Fig. 1b). Here, the generation of the excited vibrational states is provided by intra-pulse excitation with an ultra-short and spectrally broadband pump (BB-pump) pulse. Intra-pulse excitation is possible, if the Stokes pulse is shorter than the oscillation period for phonons (e.g., 24 fs for 1380 cm^{-1}), entailing that sub-20-fs pulses are needed to excite the vibrational modes up to 1300 cm^{-1} . Such a short pulse also has the advantage of being spectrally broad. This means that intra-pulse excitation over a broad frequency range is possible. For typical crystalline materials, frequencies of only up to 1000 cm^{-1} are required. To satisfy this requirement, in our experimental setup we generate sub-20-fs pulses centered at 1400 nm , which are then combined with narrowband probe pulses at 1035 nm . The spectral coverage of our pulse is shown in Fig. 1c). Another advantage of the 3C-CARS process for the investigation of solid-state crystals is the possibility of exciting low-frequency vibrational modes, where a large number of intra-pulse combinations of wavelengths is possible. Also note that a 2C-CARS process similar to Fig. 1a) is inherently present in the 3C-CARS setup as well. In the 2C-CARS process, the sub-20-fs laser acts as the broadband Stokes pulse, while the probe laser from the 3C-scheme will provide the narrowband pump and probe pulses in the 2C-scheme. However, the 3C- and 2C-CARS processes do not cover the same wavelength range at the detector since they are used to probe different regions of the vibrational spectrum. The 3C-process probes the vibrational modes from 0 up to 1400 cm^{-1} , while the 2C-regime probes the vibrational modes from 1400 cm^{-1} up to 3200 cm^{-1} . Larger spectral separation is possible by reducing the bandwidth of the broadband beam. A time-delayed operation can now readily be realized in the 3C-scheme by the introduction of a time delay between the broadband excitation and the probe pulse. As shown below, the 3C- and 2C-CARS regions are also distinguished by different temporal behaviors. Here, the 2C-regime can be fully suppressed when a sufficient time delay is introduced, while for the 3C region, first the NRB is reduced, while resonantly excited phonons can still be measured if their dephasing time is long enough. This allows to measure NRB-free spectra in the 3C-regime. Please note, that for larger time delays also the resonant contributions will eventually disappear due to their limited life-times. Therefore, a balance needs to be found,

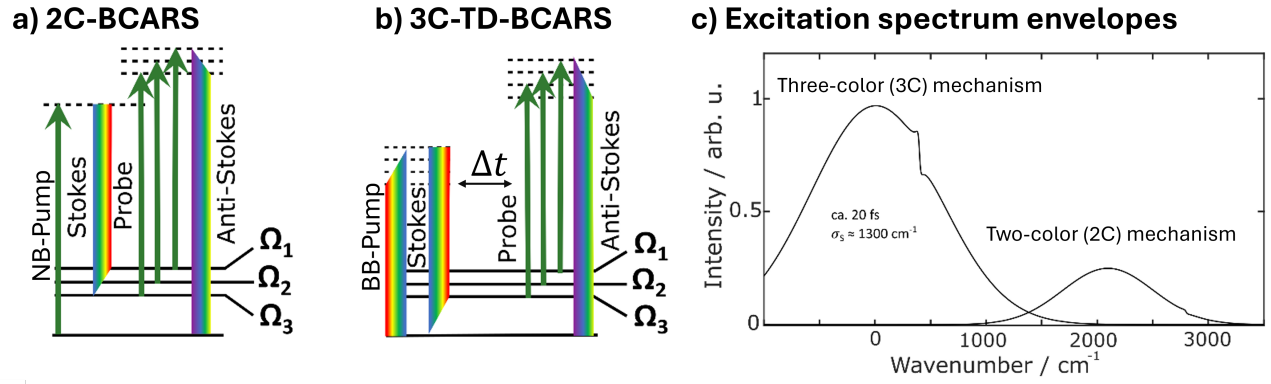


FIG. 1. Jablonski diagrams for a) 2C-BCARS and b) 3C-TD-BCARS schemes. Please note the time-delay Δt that can be introduced between the intra-pulse excitation and the probe pulse in the 3C-TD-BCARS setup. The key distinction between the 2C- and 3C-schemes are the uses of a narrowband (NB)-pump pulse in the 2C-scheme, and a broadband (BB) pump pulse in the 3C-scheme. c) Excitation envelope for a sub-20 fs Stokes pulse centered around 1400 nm and a pump laser at 1035 nm. Here, phonons with wavenumbers of up to 1300 cm^{-1} can be probed in the 3C-scheme, while 2C-spectrum is mostly separated from the 3C-region. Using an even lower probe laser wavelength or longer central wavelength for the Stokes pulse could separate the two regions even further.

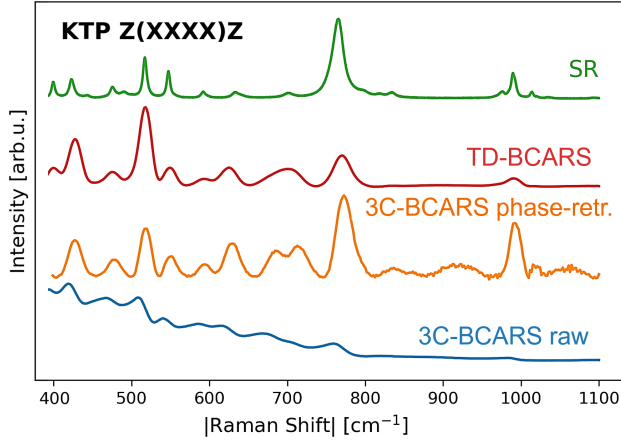


FIG. 2. The zero-time delay 3C-BCARS spectrum (blue) on KTP displays peaks down to 400 cm^{-1} , necessitating the removal of the NRB contribution for peak shape restoration by performing a phase-retrieval in-post processing²² (orange, 3C-BCARS phase-retr.). The TD-CARS measurement with a delay of 4 ps (red) demonstrates an NRB-free spectrum, eliminating the need for any post-processing. For reference, a SR spectrum of the same crystal is shown (green). Please note, that all three CARS spectra show slightly broader peak-width as compared to SR, which is a result of the spectral broadening by the natural line-width of the pulsed pump laser¹⁷. The Raman shift is given in absolute values to make the anti-Stokes BCARS signal more readily comparable with SR spectra, which are often Stokes-shifted.

where the NRB is suppressed, while sufficiently large resonant signals are measurable.

In our experimental setup described in detail in previous works^{17,18}, Δt can be varied by adjusting a mechanical delay line for the pump/probe pulses. The delay line is controlled by a micrometer screw with $10 \mu\text{m}$ increments, which translates to a 67 fs accuracy of Δt . The mechanical stage allows for

time-delay variation within a total range of 25 ps. To demonstrate the viability of NRB-suppression in the 3C-CARS configuration, measurements were conducted on a potassium titanyl phosphate (KTP) crystal using a Z(XXXX)Z (forward-) scattering configuration, with the results being depicted in Figure 2. The scattering configuration is given in an extended Porto notation¹⁶, where the outer two Z denote the vectorial direction of the excitation and scattered light in crystal axis, respectively, while the inner X denote the polarization of the anti-Stokes signal, the probe, pump and Stokes beams, respectively. In this experiment, the light is focused parallel to the z-axis into the crystal and collected in forward direction, while the polarization of all lasers and the signal are chosen to be parallel to the x-axis of the crystal.

The unprocessed 3C-BCARS data with zero time-delay (blue) showcases the pronounced intensity for low-frequency modes down to 400 cm^{-1} . This increasing intensity towards lower wavenumbers is a direct result of the intra-pulse excitation scheme, which provides more and more combinations of excitation wavelengths for smaller and smaller shifts. In principle, even lower-frequency modes are populated in the intra-pulse scheme, however, due to the filters used in the detection path of the experimental setup, a cut-off at $\sim 400 \text{ cm}^{-1}$ is observed. Note that, in principle Raman peaks down to a few 10 cm^{-1} are measurable with such a setup, which is ideal for solid-state investigations. This spectrum is then subject to NRB removal using the Kramers-Kronig (KK) transformation²² which is applied to unveil the phase-retrieved CARS spectrum (orange, 3C-BCARS phase-retrieved). In contrast, by choosing a time delay of approximately 4 ps, an NRB-free CARS spectrum can be obtained with TD-BCARS (red), eliminating the necessity for NRB removal in post processing. Notably, the relative peak intensities differ between TD-BCARS and the transformed 3C-BCARS. This disparity arises from the fact that in 3C-BCARS, the maximum intensity of each peak is measured, while in TD-CARS, the intensities of the individual modes

are reduced depending on their lifetimes. Further investigation into these lifetimes is presented below. Nevertheless, a spectrum with Lorentzian-like shapes similar to a typical SR spectrum (green) is readily obtained without the need for any processing.

TD-CARS proves to be an effective technique for experimental NRB removal and can validate the NRB removal by post-processing, for example via using the KK-algorithm. However, we must note that introducing a time delay also diminishes the intensity of the resonant component. In this case, the TD-CARS signal intensity is only 10 % of the 3C-CARS peak intensity for zero time-delay, necessitating longer acquisition times. To combine the advantages of both techniques, 3C-BCARS without time-delay could be best suited for comprehensive mapping with subsequent KK transformation, while TD-BCARS excels in single-spectrum acquisition at specific points of interest, to validate the transformation results, as well as to extract phononic dephasing times, which will be discussed below.

III. TEMPORAL PROFILE OF THE NRB

To enable an NRB-free measurement as well as to determine phonon dephasing times, it is first necessary to determine the duration of the NRB, which is mostly limited by the temporal convolution of the pulses with the instantaneous response of the NRB. For this, glass is investigated, which is an amorphous material with a frequency-independent third-order nonlinear response^{16,17}. Glass shows no distinct phonon peaks due to its nature as an amorphous substance, but only an NRB. The time-delay sweeps are displayed in Figure 3.

Fig. 3 a) shows a hyperspectral intensity map plotted with the delay time on the x-axis and the Raman shift along the y-axis. The graph displays two distinct intensity regions: the 3C-NRB in the region on the bottom up to ca. 1300 cm^{-1} , where intra-pulse excitation dominates, and the 2C-NRB region beyond approximately 1300 cm^{-1} , where the narrow-band probe laser also acts as the pump laser, while the 20-fs pulse acts as the broadband Stokes pulse. Fig. 3 b) shows exemplary intensity curves for the two regions at approximately 800 cm^{-1} (3C-NRB) and 1700 cm^{-1} (2C-NRB). Both 2C- and 3C-signals display a somewhat a bell-shaped curve, with $\Delta t = 0$ being chosen from the position of maximum intensity. Basically, the observed shape and peak is similar to a form of correlation function of the (temporal) overlap of the Stokes and pump pulses. Here, a Gaussian fit of the 2C-NRB yields a temporal FWHM of about $\tau = 2.69\text{ ps}$, while the 3C-NRB yields a width of $\tau = 3.39\text{ ps}$.

To understand the difference of almost 0.6 ps between the 2C- and 3C-NRB decay times, the temporal shapes can be estimated from the pulse durations of the Stokes and pump pulses and their interaction, respectively. Here, the NRB is expected to decay instantaneous. Therefore, the measurement is mainly broadened by the temporal width of the excitation pulse²⁸, which can be calculated as the cross-correlation of the pump, Stokes and probe pulses. For a simple estimation, both pulses are approximated with a Gaussian shape in the

temporal domain. Due to the intra-pulse excitation, the 3C intensity I_{3C} scales quadratically with the Stokes intensity I_s of the broadband Stokes pulse, which in this case acts as both BB pump and Stokes, and linearly with the probe pulse intensity I_{pr} . Hence, the convolution is calculated as:

$$I_{3C}(\Delta t) \propto (I_{pu} * I_s^2)(\Delta t). \quad (1)$$

Here, convolution of the broadband Stokes pulse (estimated to be about 20 fs) and the 3.70 ps long pump pulse yields a convoluted duration of about $\tau_c = 3.79\text{ ps}$, which is reasonably consistent with the Gaussian fit of the measured data. For the 2C-process, the intensity scales quadratically with the pump intensity, leading to a calculated convolution as:

$$I_{2C}(\Delta t) \propto (I_{pu}^2 * I_s)(\Delta t). \quad (2)$$

Consequently, from theory we estimate a Gaussian shape with an FWHM of $\tau = 2.26\text{ ps}$, which explains the FWHM of the measured 2C-NRB of $\tau_{2C-NRB} = (2.69 \pm 0.08)\text{ ps}$ to be narrower compared to the 3C-NRB duration. These calculations both underestimate the experimentally observed pulses due to the assumption of purely Gaussian pulses, while the temporal envelopes in the experiment are not ideally Gaussian-shaped. Nevertheless, the calculations explain the observed differences in decay times in the 2C and 3C-regimes.

For an experiment, this means that NRB-free and 2C-free spectra can be obtained in our setup for delays larger than approximately $\Delta t > 3\text{ ps}$.

IV. PHONON DEPHASING IN DIAMOND

With the quantification of NRB-decay time being established, the behavior of the resonant signal can be investigated. Here, a single crystal of diamond in (100)-cut is chosen. The sample is a CVD-grown diamond commercially obtained from Applied Diamond Inc., Wilmington (DE), USA. Diamond crystallizes in the eponymous diamond structure with two atoms per unit cell, which has a single three-times-degenerated optical phonon at the zone center. Hence, only a single peak belonging to this sp^3 -bond is expected³⁰. Due to the strong bond and the relatively light C atom, its expected frequency is very high for a phonon in a typical crystal at around 1336 cm^{-1} , which is at the edge of the 3C-frequency range. However, time-delayed measurements are still possible in this regime, which shows that our setup is capable of addressing most typical crystalline materials including many semi-conductors or oxides. Fig. 4 a) shows a hyperspectral map similar to Fig. 3 a). Here, again the 2C-NRB and 3C-NRB regions are visible, but also an additional, resonant sp^3 peak at 1336 cm^{-1} , which is measurable even for $\Delta t > 10\text{ ps}$. For time delays larger than 3 ps, its intensity is exclusively stemming from the 3C-process. For shorter time delays, this peak lays in the overlap regions of the 2C and 3C processes.

Figure 4 b) shows the intensity profiles in logarithmic scale as a function of time-delay for the sp^3 peak intensity and the

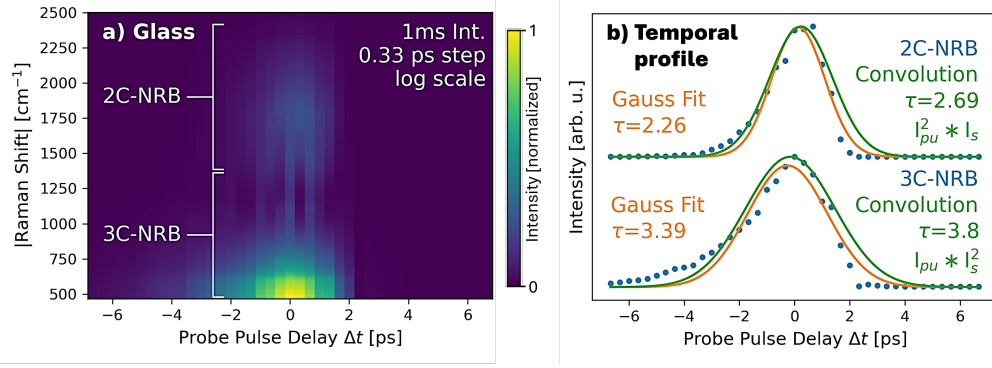


FIG. 3. TD-BCARS behavior of the NRB measured on glass: a) The spectral response shows two distinct regions, a 3C-NRB for wavenumbers approximately smaller than $<1300 \text{ cm}^{-1}$ and a 2C-NRB spanning from approximately 1300 to 2500 cm^{-1} . b) The time-dependent intensity curves can be approximated by the convolution of the 20 fs Stokes pulse I_s and the 3.8 ps pump pulse I_{pu} , which enters the process quadratically for the 2C-process, but only linearly in the 3C-process.

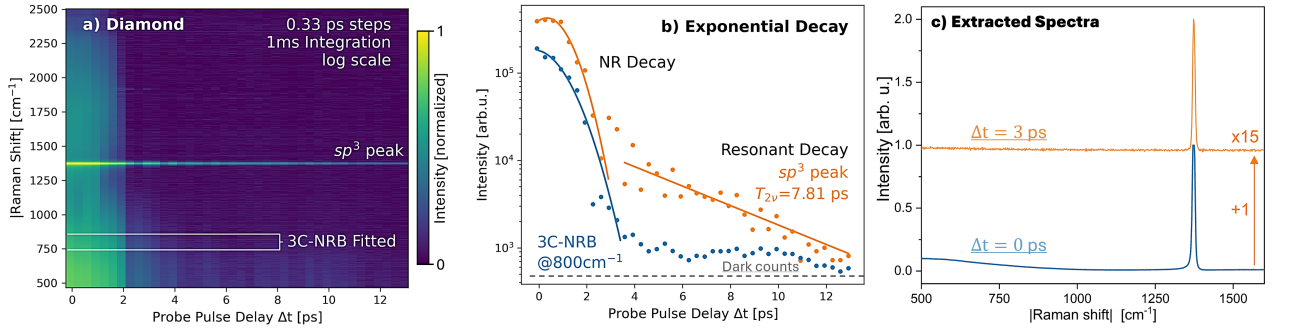


FIG. 4. TD-BCARS spectra of diamond when varying the probe pulse delay: a) The 3C-NRB and 2C-NRB decay fast, while the strong sp^3 diamond peak is measurable even at 10 ps delay. b) On a logarithmic scale, both the 3C-NRB and the sp^3 signal exhibit a Gaussian-shaped decay region, while the resonant sp^3 signal shows an additional, linear decay. c) A symmetric, Lorentz-shaped peak form can be obtained with a time-delay of 3 ps.

3C-NRB intensity around 800 cm^{-1} in orange and blue, respectively. Here, as established for glass (see Fig. 3) the NRB completely vanishes in the 3C-region within approximately 3 ps. In contrast, the intensity of the sp^3 peak first follows the behavior of the 3C-NRB (up to 3 ps of delay), but then continues as an exponential decay. This means that NRB-free spectra can be obtained for delays of $> 3 \text{ ps}$ consistent with the plots in Fig. 3b), where larger delays result in even less NRB contribution, but at the cost of a reduced resonant peak intensity.

For delays $\Delta t > 4 \text{ ps}$, the sp^3 peak can be accurately fitted using an exponential decay function³¹, which allows to determine the phononic dephasing time:

$$I(\Delta t) = I_0 e^{-2\Delta t/T_{2v}}. \quad (3)$$

Here, $I(\Delta t)$ describes the measured intensity as a function of time-delay Δt , and I_0 denotes the maximum intensity of this second decay region at $\Delta t = 4 \text{ ps}$. The T_{2v} describes the dephasing time of the vibrational coherence, which contains contributions from the vibrational population decay and the dephasing of the vibrational modes³². Please note, the decay

time T_{decay} in the time-dependent spectra is not equal to the dephasing time T_{2v} . It holds $T_{decay} = T_{2v}/2$ ³¹.

The fitting of the sp^3 signal results in $T_{2v} = (7.8 \pm 1.3) \text{ ps}$. This value falls within the reported range of diamond phonon lifetimes in the literature, which range from 5.7 to 7.0 ps³³⁻³⁵. Our measured value of T_{2v} falls in the higher range of previously measured values, indicating the high homogeneity in the CVD-grown crystals³³⁻³⁵.

V. PHONON DEPHASING IN KTP AND KTA

To demonstrate the TD-BCARS methodology on more complex crystals, we investigated a sample of z-cut potassium titanyl phosphate (KTiOPO₄, KTP) and a sample of potassium titanyl arsenate (KTiOAsO₄, KTA). KTP and KTA are isostructural crystals, which see widespread use in nonlinear and quantum optics. From the viewpoint of Raman and CARS spectroscopy, KTP and KTA are ideal model systems as they feature a 64-atom unit cell with 189 optical phonons, which are all Raman- and CARS-active³⁶⁻⁴⁰. For one polar-

ization setting of excitation and detection, typically more than 40 phonons are expected to be visible in one spectrum spanning a range from almost 0 to about 1200 cm^{-1} . The result of the broadband TD-BCARS measurement on KTP and KTA, each, is displayed in Fig. 5.

Both KTP and KTA exhibit comparable Raman spectra, as shown in Figures 5 a) and c). Interestingly, while the spectrum of KTP and KTA usually is expected to show more than 40 phonons per polarization setting, we do only see 10 to 15 peaks at a time-delay of 3 ps. Here, certain phonons may not be visible due to a fast dephasing. The hyperspectral plots in Figure 5 b) and d) illustrate a range of resonant peaks as brighter lines against the NRB. While these peaks are not as prominent as the diamond signal, an averaging over 100 spectra with 1 ms integration time enabled acquisition for time-delays of up to 8 ps. Exponential decay fitting was applied to all peaks starting from $\Delta t = 3\text{ ps}$, and the resulting dephasing times T_{2v} ranging from 2.7-7.6 ps are presented in Table I. Here, distinct differences between vibrational modes in one material are visible indicating that the dephasing time is phonon dependent. In contrast, similar features in both materials feature comparable decay times indicating systematic similarities between both materials and their phonons.

The reported dephasing times of phonons in KTP from literature⁴¹ are within the same order of magnitude. However, while the literature values range from 0.5-2.1 ps, the measured results for our corresponding modes display lifetimes of 2.9-6.3 ps. This hints at higher quality crystals in our experiment with longer phonon dephasing times. This experiment, as well as the previously discussed investigations on diamond suggest that dephasing times could be used to quantify the quality of crystals.

VI. CONCLUSION

In this work, we have employed broadband three-color time-delayed CARS, which allows to measure NRB-free broadband CARS spectra, as well as to determine phonon-dephasing times across typical vibrational frequencies observed in crystalline materials. On the one hand, we demonstrate that non-resonant background-free spectra, which is a central challenge in CARS, can be readily obtained by using the time-delayed scheme and selecting an appropriate time-delay. On the other hand, we show that TD-BCARS can be used to measure the dephasing time across the full phonon spectrum at once. The methodology is tested on amorphous SiO_2 (glass), which is used to characterize the setup-specific and material-independent response times, and applied to single crystals of diamond and the ferroelectrics KTP and KTA. We measure dephasing times on the same order of magnitude as those acquired by complementary methods in single-frequency measurements, which renders the method a valuable extension for phononic examinations of materials. Recently, coherent excitations of phonons and their dephasing times see particular interest in experiments, where resonant, optical controls are used to switch material properties, like ferroelectric domains^{42,43}. Here, our fast measurement tech-

nique of full spectra could serve as a guide for such experiments. Another possible extension of our technique could be in imaging studies of solids using time delay as a contrast mechanism, which are expected to change depending on spatial variations of crystal structure or defects.

VII. ACKNOWLEDGEMENTS

The authors gratefully acknowledge financial support by the Deutsche Forschungsgemeinschaft (DFG) through projects CRC1415 (ID: 417590517), INST 269/656-1 FUGG and FOR5044 (ID: 426703838; <http://www.For5044.de>), as well as the Würzburg-Dresden Cluster of Excellence "ct.qmat" (EXC 2147; ID: 390858490), LASERLAB-EUROPE (grant agreement no. 871124, European Union's Horizon 2020 research and innovation program), and the European Union project CRIMSON (grant agreement no. 101016923). GC and DP acknowledge financial support by the European Union's NextGenerationEU Program with the I-PHOQS Infrastructure (IR0000016, ID D2B8D520, CUP B53C22001750006) "Integrated infrastructure initiative in Photonic and Quantum Sciences". The authors thank Jiří Hlinka of the Czech Academy of Sciences, Prague, Czech Republic, for providing samples.

VIII. REFERENCES

- ¹G. F. Nataf, M. Guennou, A. Haußmann, N. Barrett, and J. Kreisel, "Evolution of defect signatures at ferroelectric domain walls in mg-doped lithium niobate," *physica status solidi (RRL) – Rapid Research Letters* **10**, 222 (2016).
- ²M. D. Fontana and P. Bourson, "Microstructure and defects probed by Raman spectroscopy in lithium niobate crystals and devices," *Applied Physics Reviews* **2**, 040602 (2015).
- ³M. Tejerina, D. Jaque, and G. Torchia, "A 2D μ -Raman analysis of low repetition rate femto-waveguides in lithium niobate by using a finite element model," *Optical Materials* **36**, 936 (2014).
- ⁴M. Tejerina, K. Pereira da Silva, A. Goñi, and G. Torchia, "Hydrostatic-pressure dependence of Raman-active optical phonons in Nd-Mg-lithium niobate," *Optical Materials* **36**, 581 (2013).
- ⁵G. Stone, B. Knorr, V. Gopalan, and V. Dierolf, "Frequency shift of Raman modes due to an applied electric field and domain inversion in lithium niobate," *Phys. Rev. B* **84**, 134303 (2011).
- ⁶A. K. Arora, M. Rajalakshmi, T. R. Ravindran, and V. Sivasubramanian, "Raman spectroscopy of optical phonon confinement in nanostructured materials," *Journal of Raman Spectroscopy* **38**, 604 (2007).
- ⁷A. Sunny and K. Balasubramanian, "Laser-induced phonon and magnon properties of NiO nanoparticles: A Raman study," *Journal of Raman Spectroscopy* **52**, 833 (2021).
- ⁸Y.-J. Sun, S.-M. Pang, and J. Zhang, "Review of Raman spectroscopy of two-dimensional magnetic van der Waals materials," *Chinese Physics B* **30**, 117104 (2021).
- ⁹M. Paillet, R. Parret, J.-L. Sauvajol, and P. Colombari, "Graphene and related 2D materials: An overview of the Raman studies," *Journal of Raman Spectroscopy* **49**, 8 (2018).
- ¹⁰E. Singh, M. N. Pionteck, S. Reitzig, M. Lange, M. Rüsing, L. M. Eng, and S. Sanna, "Vibrational properties of LiNbO_3 and LiTaO_3 under uniaxial stress," *Phys. Rev. Mater.* **7**, 024420 (2023).
- ¹¹M. Rüsing, S. Neufeld, J. Brockmeier, C. Eigner, P. Mackwitz, K. Spychala, C. Silberhorn, W. G. Schmidt, G. Berth, A. Zrenner, and S. Sanna, "Imaging of 180° ferroelectric domain walls in uniaxial ferroelectrics by

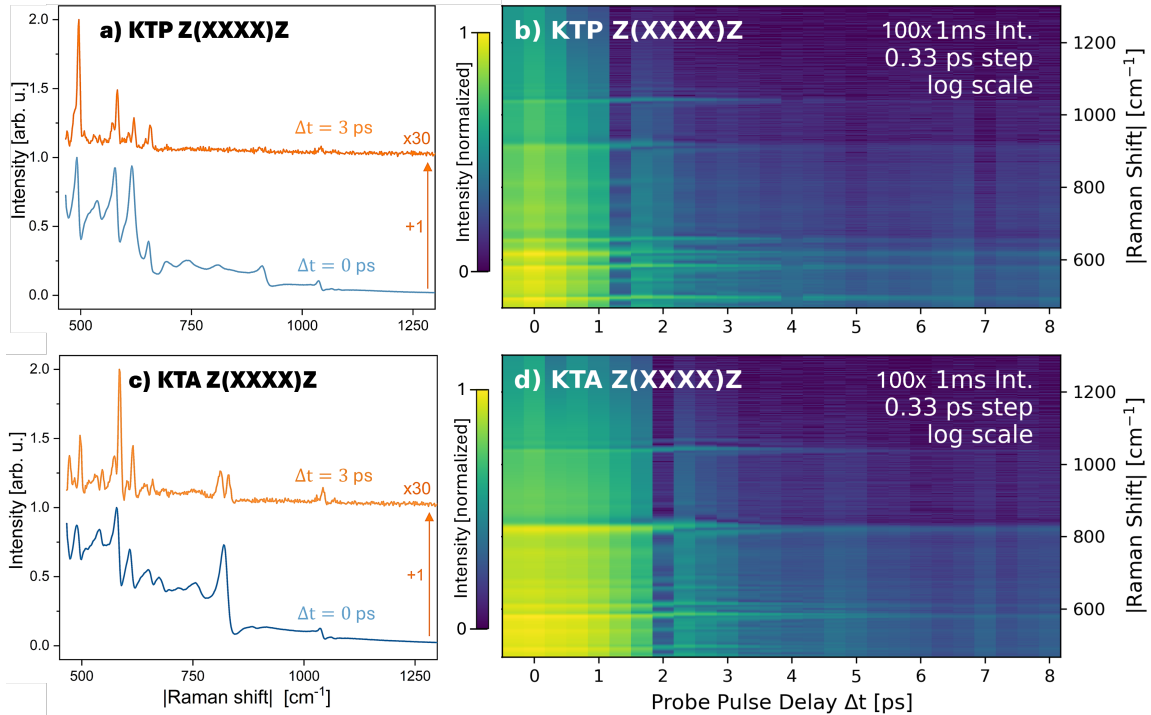


FIG. 5. TD-CARS on Z(XXXX)Z KTP and KTA: a) The KTP spectrum at $\Delta t = 0$ ps shows multiple distorted peaks, while with a delay of $\Delta t = 3$ ps yields narrow peaks similar to spontaneous Raman scattering. b) The time-delay sweep shows the dephasing of the different peaks. The related material KTA is shown as a comparison in c) and d). Extracted phonon decoherence times are shown in Tab. 1.

TABLE I. Dephasing time T_{2v} for phonons in KTP and KTA measured in Z(XXXX)Z configuration.

Assigned crystal feature ³⁶⁻⁴⁰	Decoherence time ⁴¹ [ps]	KTP		KTA	
		$\Delta\tilde{\nu}_{Peak}$ [cm ⁻¹]	T_{2v} [ps]	$\Delta\tilde{\nu}_{Peak}$ [cm ⁻¹]	T_{2v} [ps]
PO ₄ / AsO ₄	1.95 ± 0.05	469	6.2 ± 0.6	469	7.4 ± 1.7
PO ₄ / AsO ₄		496	3.1 ± 0.3	495	4.2 ± 0.7
TiO ₆		544	5.7 ± 0.7	540	5.2 ± 1.1
TiO ₆		583	3.0 ± 0.2	580	2.8 ± 0.3
TiO ₆		614	3.7 ± 0.4	620	3.9 ± 0.5
TiO ₆	0.475 ± 0.004	655	2.8 ± 0.2	657	5.0 ± 1.1
TiO ₆		680	6.1 ± 0.8	682	5.7 ± 1.3
TiO ₆		824	6.3 ± 1.0	815	7.3 ± 1.5
-	1.64 ± 0.06	917	6.5 ± 1.0	917	7.6 ± 1.7
PO ₄ / AsO ₄		1041	2.9 ± 0.3	1037	4.4 ± 0.4

confocal raman spectroscopy: Unraveling the contrast mechanism,” Phys. Rev. Mater. **2**, 103801 (2018).

¹²V. Parodi, E. Jacchetti, R. Osellame, G. Cerullo, D. Polli, and M. T. Raimondi, “Nonlinear optical microscopy: From fundamentals to applications in live bioimaging,” Frontiers in Bioengineering and Biotechnology **8** (2020).

¹³C. Zhang and J. A. Aldana-Mendoza, “Coherent raman scattering microscopy for chemical imaging of biological systems,” Journal of Physics: Photonics **3**, 032002 (2021).

¹⁴Y. Li, B. Shen, S. Li, Y. Zhao, J. Qu, and L. Liu, “Review of stimulated raman scattering microscopy techniques and applications in the biosciences,” Advanced Biology **5**, 2000184 (2021).

¹⁵S. Reitzig, F. Hempel, J. Ratzenberger, P. A. Hegarty, Z. H. Amber, R. Buschbeck, M. Rüsing, and L. M. Eng, “High-speed hyperspectral imaging of ferroelectric domain walls using broadband coherent anti-Stokes Raman scattering,” Applied Physics Letters **120**, 162901 (2022).

¹⁶F. Hempel, S. Reitzig, M. Rüsing, and L. M. Eng, “Broadband coherent anti-stokes Raman scattering for crystalline materials,” Phys. Rev. B **104**, 224308 (2021).

¹⁷F. Hempel, F. Vernuccio, L. König, R. Buschbeck, M. Rüsing, G. Cerullo, D. Polli, and L. M. Eng, “Comparing transmission- and epi-BCARS: A round robin on solid-state materials,” Applied optics **63**, 112 (2023).

¹⁸F. Vernuccio, A. Bresci, B. Talone, A. D. la Cadena, C. Ceconello, S. Mantero, C. Sobacchi, R. Vanna, G. Cerullo, and D. Polli, “Fingerprint multiplex CARS at high speed based on supercontinuum generation in bulk media and deep learning spectral denoising,” Optics express **30**, 30135 (2022).

¹⁹F. Vernuccio, E. Broggio, S. Sorrentino, A. Bresci, R. Junjuri, M. Ventura, R. Vanna, T. Bocklitz, M. Bregonzio, G. Cerullo, H. Rigneault, and D. Polli, “Non-resonant background removal in broadband CARS microscopy using deep-learning algorithms,” Scientific Reports **14**, 23903 (2024).

²⁰L. M. Malard, L. Lafeta, R. S. Cunha, R. Nadas, A. Gadelha, L. G. Cançado, and A. Jorio, “Studying 2D materials with advanced raman spectroscopy:

- CARS, SRS and TERS,” *Physical Chemistry Chemical Physics* **23**, 23428 (2021).
- ²¹S. Xu, C. H. Camp Jr, and Y. J. Lee, “Coherent anti-stokes raman scattering microscopy for polymers,” *Journal of Polymer Science* **60**, 1244 (2022).
 - ²²C. H. Camp Jr., Y. J. Lee, and M. T. Cicerone, “Quantitative, comparable coherent anti-stokes raman scattering (CARS) spectroscopy: correcting errors in phase retrieval,” *Journal of Raman Spectroscopy* **47**, 408 (2016).
 - ²³R. Muddiman, K. O’ Dwyer, C. H. Camp, and B. Hennelly, “Removing non-resonant background from broadband CARS using a physics-informed neural network,” *Anal. Methods* **15**, 4032 (2023).
 - ²⁴C. M. Valensise, A. Giuseppi, F. Vernuccio, A. De la Cadena, G. Cerullo, and D. Polli, “Removing non-resonant background from CARS spectra via deep learning,” *APL Photonics* **5**, 061305 (2020).
 - ²⁵H. A. Rinia, M. Bonn, M. Müller, and E. M. Vartiainen, “Quantitative CARS spectroscopy using the maximum entropy method: The main lipid phase transition,” *ChemPhysChem* **8**, 279 (2007).
 - ²⁶D. Pestov, R. K. Murawski, G. O. Ariunbold, X. Wang, M. Zhi, A. V. Sokolov, V. A. Sautenkov, Y. V. Rostovtsev, A. Dogariu, Y. Huang, and M. O. Scully, “Optimizing the laser-pulse configuration for coherent raman spectroscopy,” *Science* **316**, 265 (2007).
 - ²⁷R. Selm, M. Winterhalder, A. Zumbusch, G. Krauss, T. Hanke, A. Sell, and A. Leitenstorfer, “Ultrabroadband background-free coherent anti-stokes raman scattering microscopy based on a compact er: fiber laser system,” *Opt. Lett.* **35**, 3282 (2010).
 - ²⁸J. P. Ogilvie, M. Cui, D. Pestov, A. V. Sokolov, and M. O. Scully, “Time-delayed coherent raman spectroscopy,” *Molecular Physics* **106**, 587 – 594 (2008).
 - ²⁹D. Polli, V. Kumar, C. M. Valensise, M. Marangoni, and G. Cerullo, “Broadband coherent raman scattering microscopy,” *Laser and Photonics Reviews* **12** (2018).
 - ³⁰S. A. Solin and A. K. Ramdas, “Raman spectrum of diamond,” *Phys. Rev. B* **1**, 1687 (1970).
 - ³¹Y. J. Lee and M. T. Cicerone, “Vibrational dephasing time imaging by time-resolved broadband coherent anti-stokes raman scattering microscopy,” *Applied Physics Letters* **92**, 041108 (2008).
 - ³²H.-O. Hamaguchi and T. L. Gustafson, “Ultrafast time-resolved spontaneous and coherent raman spectroscopy: The structure and dynamics of photogenerated transient species,” *Annual Review of Physical Chemistry* **45**, 593–622 (1994).
 - ³³F. S. de Aguiar Júnior, M. F. Santos, C. H. Monken, and A. Jorio, “Lifetime and polarization for real and virtual correlated stokes-anti-stokes raman scattering in diamond,” *Physical Review Research* **2**, 013084 (2020).
 - ³⁴K. C. Lee, B. J. Sussman, J. Nunn, V. O. Lorenz, K. F. Reim, D. Jaksch, I. A. Walmsley, P. G. Spizzirri, and S. Praver, “Comparing phonon dephasing lifetimes in diamond using transient coherent ultrafast phonon spectroscopy,” *Diamond and Related Materials* **19**, 1289–1295 (2010).
 - ³⁵K. G. Nakamura, K. Ohya, H. Takahashi, T. Tsuruta, H. Sasaki, S. ichi Uozumi, K. Norimatsu, M. Kitajima, Y. Shikano, and Y. Kayanuma, “Spectrally resolved detection in transient-reflectivity measurements of coherent optical phonons in diamond,” *Physical Review B* **94**, 024303 (2016).
 - ³⁶M. Rüsing, C. Eigner, P. Mackwitz, G. Berth, C. Silberhorn, and A. Zrenner, “Identification of ferroelectric domain structure sensitive phonon modes in potassium titanyl phosphate: A fundamental study,” *Journal of Applied Physics* **119**, 044103 (2016).
 - ³⁷S. Neufeld, U. Gerstmann, L. Padberg, C. Eigner, G. Berth, C. Silberhorn, L. M. Eng, W. G. Schmidt, and M. Ruesing, “Vibrational properties of the potassium titanyl phosphate crystal family,” *Crystals* **13**, 1423 (2023).
 - ³⁸M. Bushiri, V. Mahadevan Pillai, R. Ratheesh, and V. Nayar, “Raman spectra of a potassium titanyl phosphate crystal in an in situ electric field,” *Journal of Physics and Chemistry of Solids* **60**, 1983 (1999).
 - ³⁹G. H. Watson, “Polarized raman spectra of potassium titanate arsenate and isomorphic nonlinear-optical crystals,” *Journal of Raman Spectroscopy* **22**, 705 (1991).
 - ⁴⁰G. E. Kugel, F. Brehat, B. Wyncke, M. D. Fontana, G. Marnier, C. Carabatos-Nedelec, and J. Mangin, “The vibrational spectrum of a potassium titanyl phosphate single crystal studied by raman and infrared reflectivity spectroscopy,” *Journal of Physics C: Solid State Physics* **21**, 5565 (1988).
 - ⁴¹H. A. S. Singhapurage, D. Senarathna, and F. Ganikhanov, “Decay of raman active vibrations within oxide groups of potassium titanyl phosphate,” *Optical Materials* **137**, 113526 (2023).
 - ⁴²P. Chen, C. Paillard, H. J. Zhao, J. Íñiguez, and L. Bellaiche, “Deterministic control of ferroelectric polarization by ultrafast laser pulses,” *Nature Communications* **13**, 2566 (2022).
 - ⁴³M. Kwaaitaal, D. G. Lourens, C. S. Davies, and A. Kirilyuk, “Epsilon-near-zero regime enables permanent ultrafast all-optical reversal of ferroelectric polarization,” *Nature Photonics* **18**, 569 (2024).